

## Optical State Estimation Using Wavefront Data

David Redding,<sup>a</sup> Norbert Sigrist,<sup>a</sup> John Z. Lou,<sup>a</sup> Yan Zhang,<sup>a</sup> Paul Atcheson,<sup>b</sup> Scott Acton,<sup>b</sup> William Hayden<sup>c</sup>

<sup>a</sup>Jet Propulsion Laboratory, California Institute of Technology, Pasadena CA 91109

<sup>b</sup>Ball Aerospace, Boulder CO

<sup>c</sup>NASA Goddard Space Flight Center, Greenbelt MD

### ABSTRACT

The use of wavefront measurements to deduce the state of multiple optics in a telescope beam train – their misalignments and figure errors – can be confused by the fact that there are multiple potential sources for the same measured error. This talk applies Kalman filtering techniques as a tool for separating true telescope errors from artifactual testing errors in the alignment and testing of NASA's James Webb Space Telescope, a large segmented-aperture cryogenic telescope to be launched after 2010.

Keywords: optical testing, segmented mirror, space telescope, wavefront control, wavefront sensing, state estimation

### INTRODUCTION

The testing of an optical system often involves the introduction of test-specific optics, such as collimators, autocollimating flats, light sources, null lenses, interferometers and the like. These test optics bring additional sources of aberration – aberrations that are easily confused with errors in the target optical system. For small systems tested in stable laboratory conditions, the test-optics aberrations may be calibrated and removed from the test data. For large telescopes, identifying and separating the (perhaps time-varying) aberrations of the test optics from the target system is more challenging. This is especially true for light-weight, cryogenic space telescopes such as the James Webb Space Telescope, where the test may occur in conditions that are significantly different from its on-orbit environment, and where the sheer size of the telescope (6.5 m aperture) makes independent calibration of the test optics difficult or impossible.

This paper presents a testing methodology, based on optimal estimation theory, that provides a rigorous framework for identifying and separating errors in the test optics from those in the target system. It provides a method for combining all test data, including component test data, alignment metrology, as well as wavefront measurements and other metrology taken during an extended test sequence, to produce an optimal estimate of the state of all of the optics. This method utilizes knowledge of the measurement errors, actuation errors, and prior knowledge errors to optimally combine the various sources of information. It provides estimate “error bars” as well as the estimates themselves.

The application of interest is the testing of the James Webb Space Telescope (JWST) at the NASA Plum Brook, Ohio, cryogenic vacuum facility. JWST is an 18-segment, 6.5 m segmented-aperture, cryogenic, space telescope for visible and infrared astronomy. JWST is an actively controlled telescope, meaning that the primary mirror (PM) segments and the secondary mirror (SM) are equipped with actuators, and can be adjusted to correct some aberrations after launch. JWST, which is scheduled for launch early in the second decade of this century, will extend our scientific reach into the period of the formation of the earliest galaxies. It will have sufficient sensitivity, resolution and field to perform a deep-field observation many times faster and deeper than the Hubble deep field observations.

The JWST Wavefront Sensing and Control (WFS&C) system provides limited correction of aberrations after launch.<sup>1,2,3</sup> Each of the 18 segments is equipped with 7 Degrees-of-Freedom (DOF) of actuation: tip, tilt and twist rotation; X and Y-decenter and piston translation; and focus correction. This system permits correction of segment deployment errors. It provides limited correction of segment Radius of Curvature (RoC) and astigmatism errors also.

## MODELING JWST AT PLUM BROOK

JWST will be integrated and tested in the huge cryogenic vacuum chamber at Plum Brook. This facility was chosen for its large size and its relatively quiet seismic environment. When equipped with He and N<sub>2</sub> shrouds, it should permit operation of JWST at approximately orbital temperatures. JWST will be suspended from a tower, with the telescope facing down, and sensitive elements supported by gravity off-loading mechanisms. The greatest deviation from orbital conditions is the fact that the testing will be done in gravity.

In this study we consider the testing of the JWST Optical Telescope Element (OTE) prior to installation of the various science instruments. The OTE is our “target system,” and consists of the PM, SM, a Tertiary Mirror (TM), a Fine Steering Mirror (FSM) and a pupil mask located very near the FSM, at an image of the PM entrance pupil. The “test optics” consist of a set of Auto-Collimating Flats (ACFs) arranged for an autocollimation test. Metrology will be provided during the test by 2 multi-color interferometers, one located at the center of curvature of the PM and observing PM figure; the other located in the Integrated Science Instrument Module (ISIM) and observing the OTE beam train in double-pass. The interferometers will operate nearly continuously, with information taken nearly simultaneously. The test setup is sketched in Fig. 1.

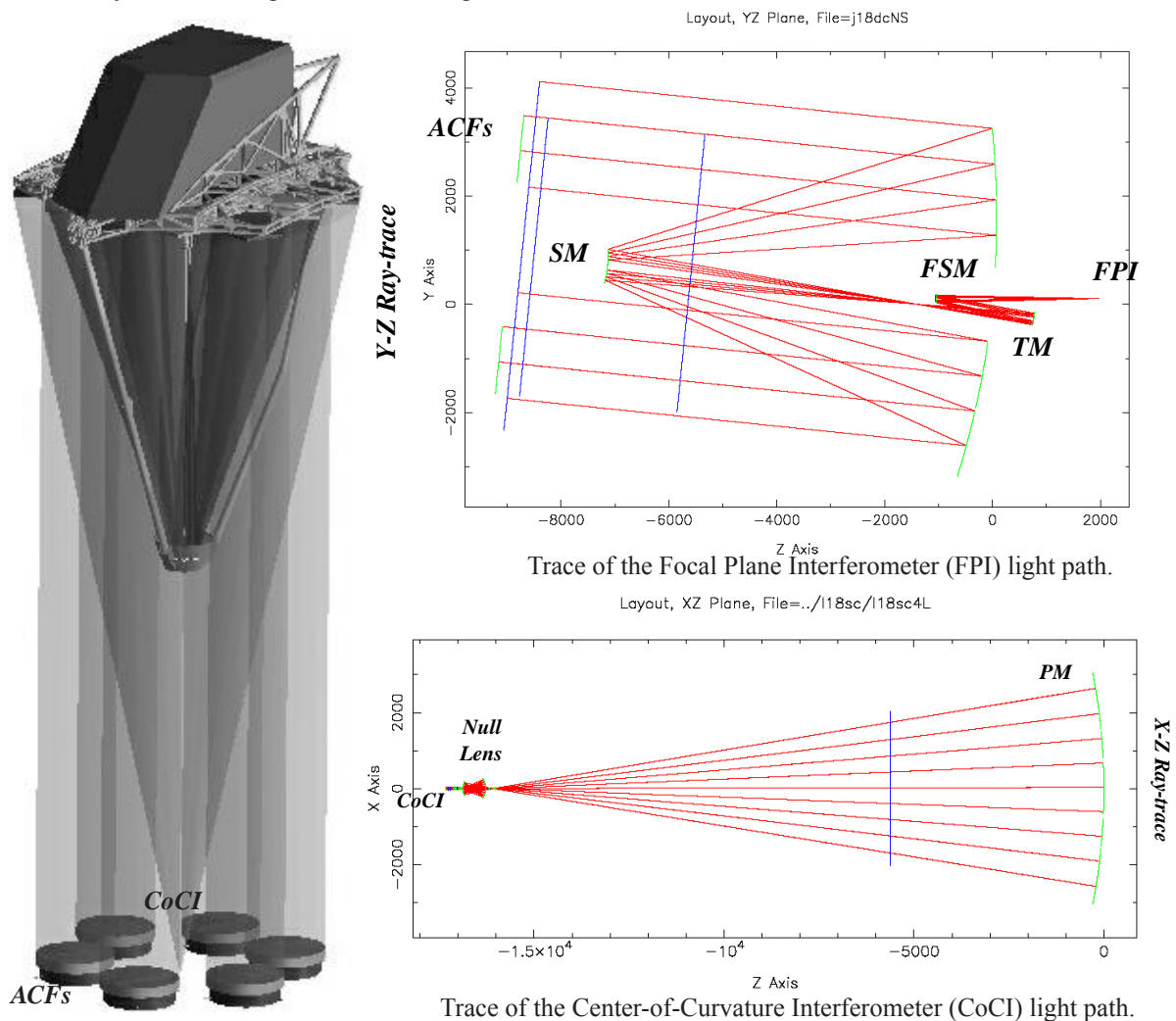


Fig. 1. Testing the JWST OTE, showing 2 light paths. The CoC Interferometer (CoCI) monitors the PM figure from the PM center of curvature. The Focal Plane Interferometer (FPI) measures the entire telescope in double pass, using the sub-sampled aperture ACFs to return light.

Perhaps the best way to visualize the test is to examine the effect of the various DOFs on the interferometer wavefronts. For example, displacing one of the segments in the local piston DOF causes a hexagonal step discontinuity in the PM figure, as seen in the CoC WF, while the effect in the FP WF is a “pie-shaped,” truncated hex displacement. More examples are provided in Figs. 2 and 3, which show the wavefronts of both light paths as optical path-difference (OPD) matrices, evaluated at the exit pupils of the CoC and FP interferometers.

There are a total of 369 optical DOFs of primary interest, including displacement, rotation and deformation DOFs for each element of the telescope and each test optic. We term these DOFs the optical state, and organize them into a long column vector  $x$ , so that each element of  $x$  is a perturbation value for a particular optical DOF, as summarized in Table 1. Not every DOF affects both light paths. The CoC light path is not influenced by the telescope optics other than the PM segments, and the FP light path is unaffected by perturbations of the null lens. The PM DOFs are common to both, but affect them differently, as is illustrated in Fig. 4.

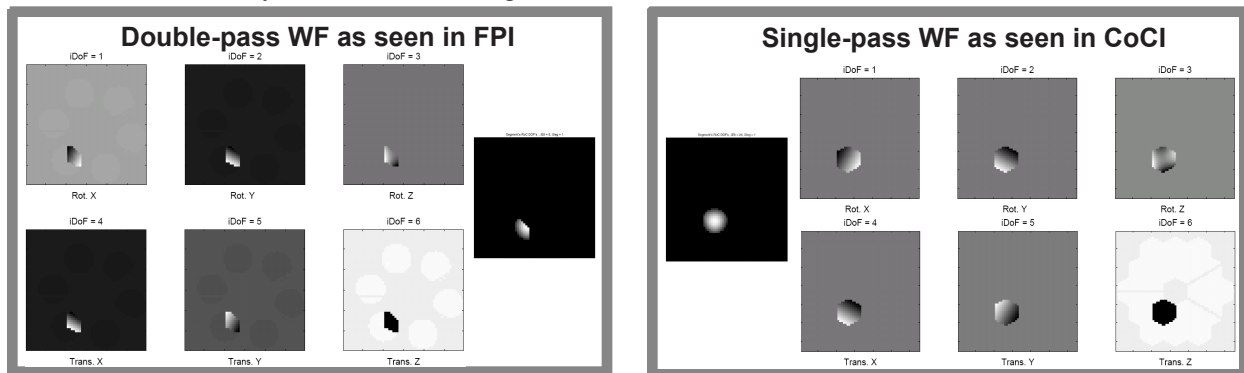


Fig. 2. Wavefronts seen at the CoC and FP interferometers in response to PM segment rigid-body and RoC DOFs.

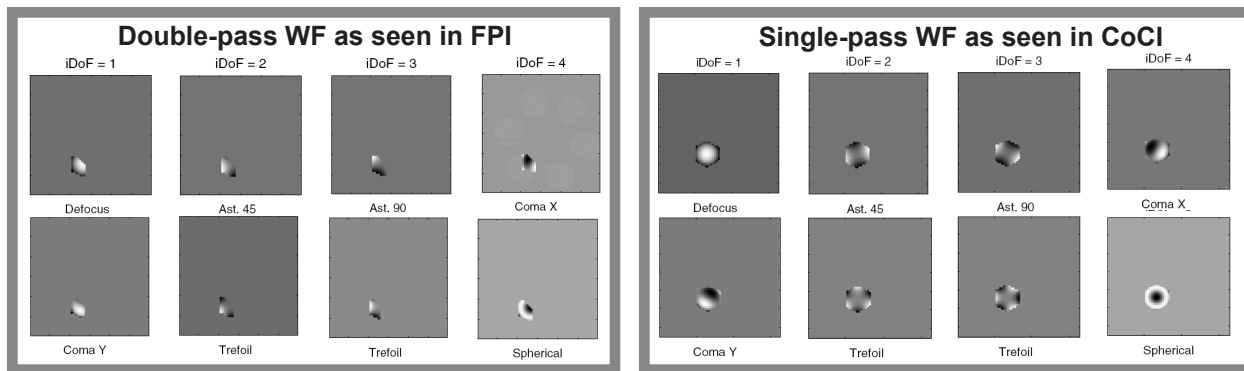


Fig. 3. Wavefronts seen at the CoC and FP interferometers in response to PM segment deformation DOFs.

Table 1: Degrees of freedom and initial state error standard deviations for the 369 elements of  $x$ .

DOF	Initial Std Dev	DOF	Initial Std Dev
Segment tilt	200 urad	Null lens	6 nm
Segment twist	286 urad	TM tilt	100 urad
Segment decenter	100 um	TM decenter	10 um
Segment piston	200 um	TM piston	10 um
Segment RoC	10 nm	FSM tilt	100 urad
Segment deformation	20 nm/mode for 8 Zernike modes	FSM decenter	10 um

Table 1: Degrees of freedom and initial state error standard deviations for the 369 elements of  $x$ .

DOF	Initial Std Dev	DOF	Initial Std Dev
ACF tilt	100 urad	FSM piston	10 um
ACF piston	100 um	Segment actuator tilt	10 nrad
ACF deformation	25 nm/mode	Segment actuator piston	5 nm
SM tilt	200 urad	SM actuator RoC	5 nm
SM decenter	20 um	ACF actuator tilt	1 urad
SM piston	20 um	ACF actuator piston	1 um
SM deformation	4 nm/mode	WFS error (lo/high)	1 nm / 30 nm

These simulated WFs were generated using a computer model, which traces rays simultaneously through both light paths, from the sources to the interferometer exit pupils, where they are detected. The path length of each ray represents the phase of the corresponding small patch of the entire wavefront, and (after subtracting the mean) is recorded as an entry in the WF matrix WCoC or WFP. The model was written using the MACOS<sup>4</sup> optical modeling code, linked as a function to the Matlab<sup>TM</sup> analysis software.

The model has 2 main purposes. The first is to provide a simulation of the test, which we use as a substitute for the real thing as we develop test procedures. Here we generally use the full nonlinear ray-trace and kinematics of the MACOS model. The second purpose is to provide a model for use in the estimation and control algorithms. For this purpose, a linearized version of the full model is especially useful.

The linearized model consists of 2 matrix equations: the *measurement equation*, which defines the way the optical state affects the interferometric wavefront measurements; and the *state transition equation*, which governs the evolution of the optical state forward in time. The measurement equation can be generated by differentiating the ray-trace model, either analytically<sup>5</sup> or through numerical differentiation.

Rather than working directly with the Optical Path-Difference (OPD) matrices  $W$ , it is convenient to reorder the matrices into column-vector form, by stacking successive columns of the  $W$  matrices. The wavefront vectors are denoted  $w_{CoC}$  and  $w_{FP}$ . The 2 forms of the WF are related simply by:

$$w = \text{vector}(W) \quad (1)$$

$$W = \text{matrix}(w) \quad (2)$$

The measurement equation is then formed as:

$$w_i = \begin{bmatrix} w_{CoC} \\ w_{FP} \end{bmatrix}_i = \begin{bmatrix} \frac{\partial w_{CoC}}{\partial x} \\ \frac{\partial w_{FP}}{\partial x} \end{bmatrix}_i x_i + \begin{bmatrix} v_{CoC} \\ v_{FP} \end{bmatrix}_i = \frac{\partial w}{\partial x} \cdot x_i + v_i \quad (3)$$

Here the subscript  $i$  denotes the  $i^{\text{th}}$  time step in the simulation time sequence, where each subsequent value of  $i$  is some  $\Delta t$  after the preceeding. The time interval  $\Delta t$  is not necessarily constant, and the various sensitivity matrices may change as different measurements are taken. The  $v_i$  is the noise in the  $i^{\text{th}}$  measurement, or the WF sensing error. The dimension of  $x$  is several hundred, and the dimension of  $w$  is several thousand, so the partial derivative matrices  $\partial w / \partial x$  are quite large.

The  $\partial w / \partial x$  are the *sensitivities* of the WF to variations in the optical state. A simple algorithm for generating the sensitivities is to “poke” each DOF in succession, recording the resulting WF matrix, subtracting the nominal WF, and

normalizing by dividing by the poke value. This yields an approximation to  $\partial W / \partial x$  for that DOF. Applying the vector operator to  $\partial W / \partial x$  results in a column vector version,  $\partial w / \partial x_j$ , which forms the  $j^{\text{th}}$  column of the full  $\partial w / \partial x$  matrix. This algorithm works with the model or with actual hardware.

WF measurements will be made using multi-color interferometers that combine measurements at multiple wavelengths to achieve long synthetic wavelengths for the resolution of  $2\pi$  ambiguities in the WF. This feature is used for measuring the relative piston of the various segments. Performance is projected to provide large capture range (many  $\mu\text{m}$ ) and high accuracy (nm). In this study we use different values for WFS error, depending on the average piston error (low or high, as per Table 1).

The state transition equation governs the evolution of the state between measurements, which in the actual test will be driven by environmental factors and by control actuations. In a complete model, the transition equation would include structural and thermal models, and would be driven by environmental states or forcing functions. Once the telescope and test structures are designed, we will adopt such a model. In the mean time, we are taking a statistical, requirements-level approach where all disturbances are random but limited. The transition equation takes the form:

$$x_{i+1} = \frac{\partial x_{i+1}}{\partial x_i} x_i + \frac{\partial x_{i+1}}{\partial u_i} (u_i + \delta u_i) + \xi_i = x_i + \frac{\partial x_{i+1}}{\partial u_i} (u_i + \delta u_i) + \xi_i \quad (4)$$

In our case, where change in the optical state is noise and control driven, the transition matrix  $\partial x_{i+1} / \partial x_i$  is simply the identity. State-vector “drift” is driven by the process noise  $\xi$ , which is a gaussian random vector that will tend to drive the states in a random walk. The values of  $\xi$  are randomly selected for each  $i$ , with standard deviations consistent with the amount the states can be expected to change, regardless of the cause, over that time interval.

Control actuations are  $u_i$ , with noise  $\delta u_i$ . Only a subset of the states are directly actuated. Within the OTE these are the PM segment rigid-body DOFs, the PM RoC, the 5 SM DOFs, and 2 FSM DOFs. These DOFs are actuated using single-axis linear devices arranged in hexapod configuration. These actuators are capable of high-precision control. Within the test optics, the ACF tip, tilt and piston are controlled. These actuators are less precise, which presents certain challenges discussed later on. JWST hexapod kinematics and control have been analyzed previously<sup>6</sup> and are ignored in this study. The control influence matrix  $\partial x / \partial u_j$  is essentially a selection matrix, mapping the controls into the state.

In simulations, the values of  $x$  with time are determined by initializing  $x = x_0$  with values consistent with the required alignment and figure quality of the telescope and test optics. The subsequent values of  $x_i$  are computed by integrating the transition equation forward in time using Eq. 4. At each time step, new state noise values are added, and new controls (with corresponding actuator errors) may be added based on the measured  $w$  for that time.

The initial state errors  $x_0$  are determined from the specifications and requirements governing the fabrication and assembly of the OTE and test optics. These specifications provide error standard deviation values for each of the DOFs based on anticipated assembly tolerances and figure residuals, as per Table 1. In this work we assume that the errors in  $x$  and  $u$ , the process noise  $\xi$ , and the measurement errors  $v$ , are gaussian random variables. We assume that they are zero mean, based on incorporation of all known errors (such as gravity sag) into the underlying models. With these assumptions, particular realizations of the initial state vector can be computed using a Gaussian random number generator. The overall process defined by these assumptions and Eq. 4 is a Markov process.<sup>8</sup>

The process noise  $\xi$  drives the growth of the state  $x$  with time. Typical values of  $\xi$  are listed in Table 2. The error statistics driving  $x_0$ ,  $\xi$ ,  $\delta u$  and  $v$  are important non-deterministic parts of both the linear and nonlinear models. By creating many realizations of these values consistent with their assumed statistics, simulating the test for each realization, and then taking statistics on all of the results – *Monte Carlo analysis* – we can develop a statistical understanding of the performance of the test.

We can also use extensions of Eqs. 3 and 4 to propagate the *covariance* of the state vector directly, and in that way to evaluate the statistical performance of the test in a single evaluation – rather than the many cases required in Monte Carlo analysis. This *covariance analysis* approach allows the direct propagation of the standard deviation of  $x$  for a particular test sequence. Covariance analysis also underlies the formulation of the Optical State Estimator.

Table 2: Components of drift: typical values for the process noise  $\xi$ .

DOF	$\xi$ value	DOF	$\xi$ value
ACF tilt	1 urad/measurement	ACF piston	1 um/measurement
PM segment tilt	0	PM segment piston	0

For a linear gaussian random vector  $x$ , the following general transformation holds.<sup>8</sup> If a vector  $y = Hx$ , then  $y$  is also a linear gaussian random vector, with covariance  $Y$ , where

$$Y = HXH^T. \quad (5)$$

In general we will denote the covariance of a random vector as the capital letter of that variable. Thus  $\text{cov}(x) = X$ ,  $\text{cov}(w) = W$ ,  $\text{cov}(v) = N$ . Also,  $\text{cov}(\delta u) = U$ ,  $\text{cov}(\xi) = \Xi$ , etc. Applying the rule of Eq. 5 to Eq. 4, we get the state covariance transition equation:

$$X_{i+1} = X_i + \frac{\partial x}{\partial u_i} U_i \left[ \frac{\partial x}{\partial u_i} \right]^T + \Xi_i \quad (6)$$

This is a discrete Lyapunov equation.<sup>8</sup> The covariance of the  $i^{\text{th}}$  wavefront is:

$$W_i = \frac{\partial w}{\partial x} \cdot X_i \cdot \left[ \frac{\partial w}{\partial x} \right]^T \quad (7)$$

The corresponding RMS WF error is

$$WFE_i = \sqrt{\text{trace}((W_i)/n_{ray})} \quad (8)$$

Here  $n_{ray}$  is the number of WF samples.

## TWO METHODS OF CONTROL

The controls  $u$  can be determined from the wavefront measurements  $w$  in 2 differing ways. The first is by direct feedback of  $w$ . In this method, no effort is made to determine whether a particular WFE component is due to errors in figure or alignment, or whether it is due to one or another element. A WF-feedback control law is:

$$u = -Gw \quad (9)$$

$$G = \left[ \frac{\partial w}{\partial x} \cdot \frac{\partial x}{\partial u_i} \right]^+ \quad (10)$$

Here the super “+” signifies the pseudo-inverse, necessitated because there are many more WF samples than control DOFs, and usually implemented using Singular-Value Decomposition techniques.<sup>7</sup> This general form can be applied to different selections of control DOFs  $u_i$ . For instance,  $u_i$  might include only the PM DOFs, and  $w$  might be just  $w_{CoC}$ , to implement a control that sets the PM independently of the rest of the OTE.

The second method of control is to use “state feedback,” where some of the values of  $x$  are explicitly estimated, and then directly compensated through the control. This more subtle approach permits effective control of DOFs, such as SM misalignments, that the first method could not distinguish from errors elsewhere in the optical train.

## THE OPTICAL STATE ESTIMATOR

The function of the Optical State Estimator (OSE) is to take in all of the data available concerning the test, and to process that data to determine the underlying optical state  $x$  of the test. The available data includes all of the pre-test component measurements, which are folded into the “as-built” model of the system. It includes all of the WF



measurements made during the test (which will be many). It also includes knowledge of the level of error in the component and wavefront measurements:  $X$  as well as  $x$ ;  $W$  as well as  $w$ . Also known is the covariance of the measurement and actuator errors, and the covariance of the process noise.

With this information, formally optimal estimates can be made using Kalman Filter techniques.<sup>8</sup> The Kalman Filter (KF) is a Maximum-Likelihood linear system estimator in recursive form, which allows it to produce estimates that are optimal at the time each new measurement is taken, while preserving the value of all previous measurements. It is a powerful tool, used in applications such as flight control that require the mixing of data from diverse sources to produce precise current state estimates. It is perhaps underutilized in optics. We will not derive the KF here, as there are several excellent texts on the subject.

The KF is a “predictor-corrector” estimator, where at each measurement we make a *prediction* of the measurement, based on the information we had at the last measurement, and compare that to the actual current measurement. The difference of the predicted and actual measurements, termed the *innovation*, is multiplied by a gain matrix and fed back to update the estimate. The gains are weighted by the covariances of the measurement and prior-estimate errors, so as to achieve an optimal blending of prior and current information.

The prediction is made by taking the estimate computed at the preceding time step and simply projecting it forward in time using Eq. 4. We know the value of the control we commanded, so that goes into the prediction as well. The predicted measurement is then calculated by projecting the predicted state to the WF space using Eq. 3. Denoting the predicted state at time  $i$  with an over-bar as  $\bar{x}_i$ , and the estimated state with a hat, as  $\hat{x}_i$ , the predicted state is:

$$\bar{x}_{i+1} = \hat{x}_i + \frac{\partial x}{\partial u_i} u_i + \xi_i \quad (11)$$

The predicted measurement  $\bar{w}_i$  is thus:

$$\bar{w}_i = \frac{\partial w}{\partial x_i} \bar{x}_i \quad (12)$$

The new state estimate is simply the prediction plus the innovation weighted by a gain matrix  $K_i$ :

$$\hat{x}_i = \bar{x}_i + K_i(w_i - \bar{w}_i) \quad (13)$$

The gain balances the contribution of the innovation to the current estimate as the ratio of the error in the predicted state, as captured in the predicted-state covariance  $P_i$ , to the error in the measurement projected back to the state space via the transpose of the measurement matrix. We treat the actuator commands as known signals with a “measurement error” equal to the actuation noise projected to the WF space.<sup>9</sup> The error in the measurement is the covariance matrix  $R_i$ , which includes the WF measurement error and the actuation error. The gain is:

$$K_i = P_i \left[ \frac{\partial w}{\partial x_i} \right]^T R_i^{-1} \quad (14)$$

The measurement error covariance, which captures the uncertainty in both the actuation and the measurement, is:

$$R_i = \frac{\partial w}{\partial u_i} U_i \left[ \frac{\partial w}{\partial u_i} \right]^T + N_i \quad (15)$$

The error in the estimate  $\hat{x}_i$  is captured by its covariance  $P_i$ , which combines the measurement and predicted-state error covariances  $R_i$  and  $M_i$  in the state space, as:

$$P_i = \left( \left[ \frac{\partial w}{\partial x_i} \right]^T R_i^{-1} \frac{\partial w}{\partial x_i} + M_i^{-1} \right)^{-1} \quad (16)$$

The covariance of the predicted state  $\bar{x}$  is computed based on the covariances of the error in the previous estimate, projected forward to the current time:

$$M_{i+1} = P_i + \frac{\partial x}{\partial u_i} U_i \left[ \frac{\partial x}{\partial u_i} \right]^T + \Xi_i \quad (17)$$

For gaussian normal random processes, the KF estimator of Eq. 13 produces optimal estimates, in the sense that they make the best possible use of the available information, producing estimates with minimal error. In fact, the KF defines the Cramer-Rao bound for such processes.<sup>8</sup> In practical problems the KF assumptions are not always precisely met. The statistics of the processes may not be normal or stationary, the plant may not be truly linear. Many extensions to the KF have been developed to deal with specific situations of this type. However, for small deviations from the assumptions underlying the KF, the KF provides an excellent, though not precisely optimal, tool.

To illustrate the effect of the gain matrix  $K$  in balancing prior estimates versus current measurements, it is useful to consider 2 extreme cases. The first case occurs when the error in the prior estimate is very small and very much smaller than the measurement noise, so that  $P_i \rightarrow 0$ . Then

$$K_i \rightarrow 0 \quad (18)$$

and the estimate is simply the prediction:

$$\hat{x}_i \rightarrow \bar{x}_i \quad (19)$$

The other extreme case occurs when the combined measurement noise is very much less than the error in the prior estimate. The gain (Eq. 14) can be rewritten using the inversion lemma as:

$$K_i = P_i \left[ \frac{\partial w}{\partial x_i} \right]^T R_i^{-1} = P_i \left[ \frac{\partial w}{\partial x_i} \right]^T \left( R_i + \frac{\partial w}{\partial x_i} P_i \left[ \frac{\partial w}{\partial x_i} \right]^T \right)^{-1} \quad (20)$$

Now when  $R_i \rightarrow 0$ ,

$$K_i \rightarrow \left[ \frac{\partial w}{\partial x_i} \right]^{-1} \quad (21)$$

and the estimate (for an invertible plant) inverts the measurement equation.

Equations 11 to 17 are a complete expression of the OSE for JWST testing. The equations are reapplied multiple times in each test, but with different matrices, as the conditions and measurements change. These changes come if we perform measurements without control, or control without a measurement, or if we make a partial measurement (CoC only, for instance). The matrices may also change during the test if we choose to recalibrate.

The OSE can be improved and extended, by post-processing all of the data utilizing smoother techniques,<sup>8</sup> by incorporating plant nonlinearities into the filter, or in other ways. These will be investigated.

## TEST PROCEDURES, AND AN EXAMPLE

An example best illustrates the effectiveness of the OSE in estimating the optical state of JWST at Plum Brook. Here we will run through a single simulated test, where the OTE has been installed and aligned to the tolerances specified in Table 1. In broad strokes, the test procedures are as follows:

1. Initial condition. The OTE is aligned to tolerances as per Table 1. A tilt-acquisition step is performed, using optical feedback to drive the segments to return light to the CoC interferometer. The segments are deformed by gravity sag (this effect is included in the model and amounts to about 65 nm RMS). An illustration of the WFs for both light paths is provided in Fig. 4, which also shows the "estimated WF," which is the projection of the post-measurement state estimate to the WF space:

$$W_{esti} = \text{matrix} \left( \frac{\partial w}{\partial x} \hat{x}_i \right) \quad (22)$$

2. Between and during each control step, the optical alignments drift slightly (as per Table 2). To keep estimation error



small, measurements continue (but are not all shown in the figures).

3. The first control step is to align and correct the RoC of the PM segments using the CoC interferometer. The effect of this is to reduce the CoC WF (after several iterations of control) to about 281 nm, which is the limit imposed by the gravity sag errors. The FP WF remains large, as the ACF phasing is not corrected. WF estimation error is quite small, as the measurement errors are assumed to be small. Results are shown in the center columns of Fig. 4.

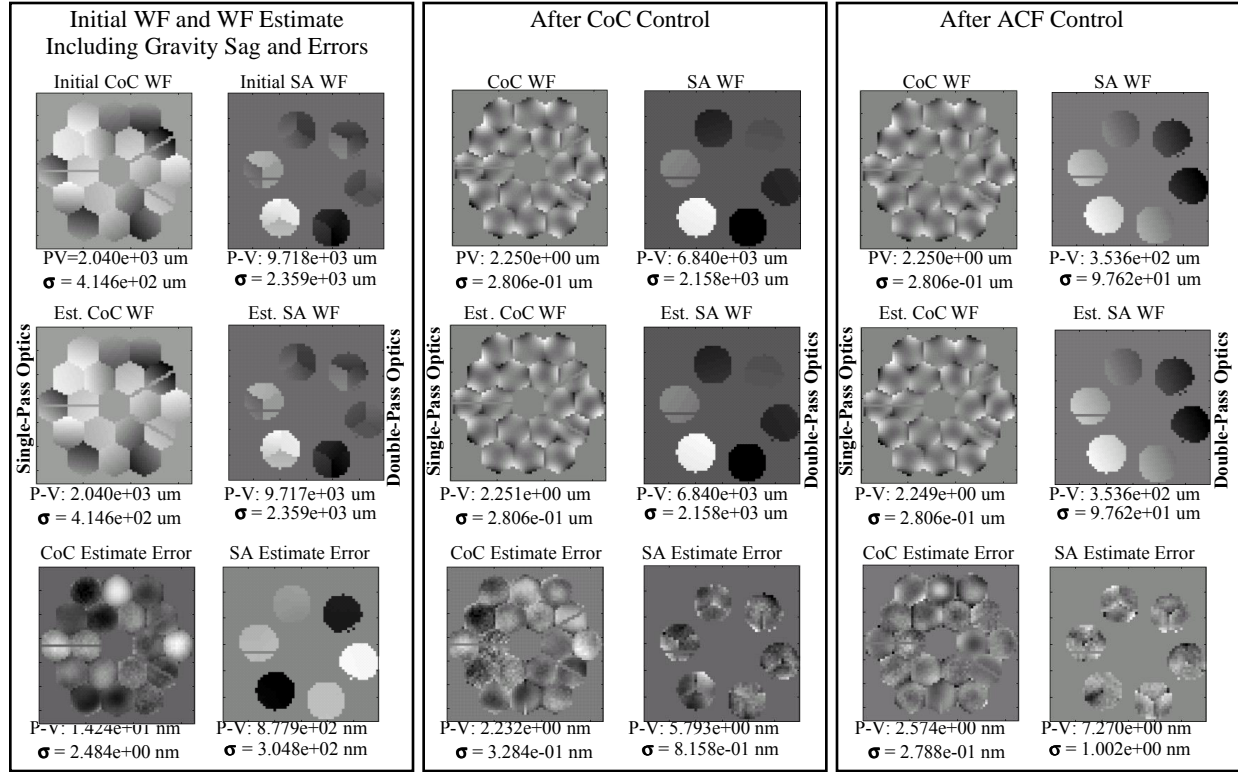


Fig. 4. Wavefront plots, showing the actual WF (top row), estimated WF (middle row), and estimate error (bottom row) as the simulated test proceeds. The estimated WFs are computed from the estimated state via the measurement equation.

4. The second control step is to set the ACFs in tip, tilt and piston using the FP interferometer. The ACF actuation error is quite large, so while the post-ACF control FP WF error is reduced substantially, it remains well outside target levels. The CoC WF is not affected by this control(Fig. 4).
5. The third control step is a “tweak” adjustment of the SM and FSM. Further drift occurs – but the estimate error remains small (Fig. 5 left column).
6. The final control step uses the segment actuators to null the WF in the FP light path. This has the effect of dephasing the CoC light path, as the segments move in “triads” to control the FP piston errors. Again, with small measurement errors, the estimated WF errors are quite small (Fig. 5 center column).
7. To determine the fundamental accuracy of the estimation process, we project the OTE state estimates to “on-orbit” conditions using a third optical model, which represents the single-pass, full telescope errors on orbit:

$$W_{\text{On-Orbit } i} = \text{matrix} \left( \left[ \frac{\partial w}{\partial x} \right]_{\text{On-Orbit}} \hat{x}_i \right) \quad (23)$$

The low error of the on-orbit prediction errors (22.4 nm RMS) verifies that the OTE errors have been successfully unravelled from the test optic errors. The small residuals are well within the control spatial-frequency bandpass and stroke limits, so the post on-orbit WFC errors will be smaller yet.

The effect of the test on the state estimate error is shown for each DOF in Fig. 6 As shown, the error in most states is reduced very dramatically. Some states are not well estimated, but those are DOFs that do not significantly impact the

WFs, and so are not DOFs we care much about. As a general rule, if the optical test measures the quantity of ultimate interest (such as WFE), the OSE will estimate those errors that are of concern.

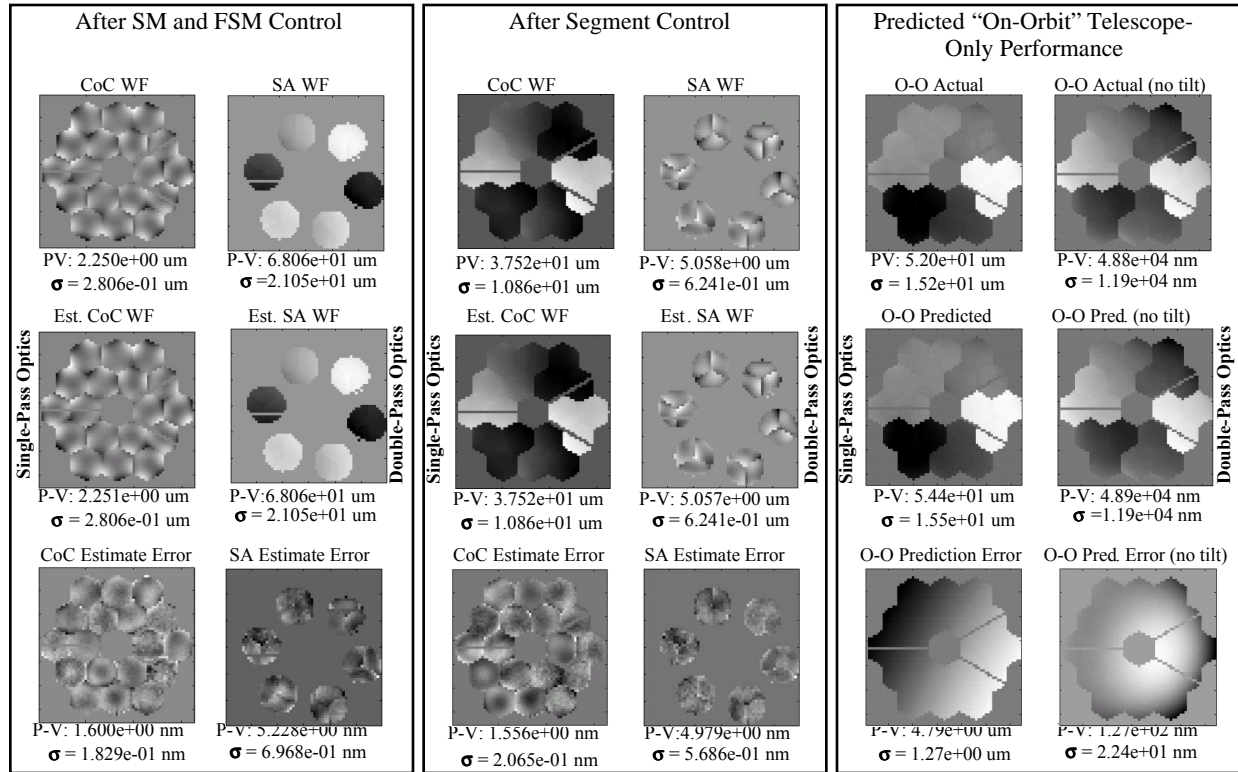


Fig. 5. Wavefront plots, showing the actual WF (top row), estimated WF (middle row), and estimate error (bottom row) as the simulated test concludes. The "on-orbit" predicted performance shows that the OTE and test optics errors have been well separated, so that the tilt-removed prediction error is only 22.4 nm.

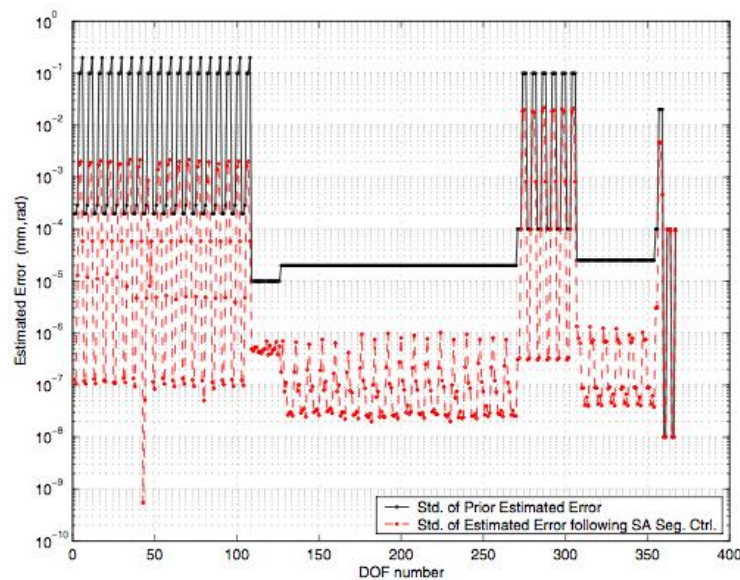


Fig. 6. State estimate error at the beginning and end of the test. The error in optically-active states has been reduced dramatically, consistent with the performance illustrated in Fig. 5. States that affect the optical performance weakly are less well estimated.

## MONTE CARLO ANALYSIS

In the single example of Figs. 4-6 we accurately estimated  $x$  using measurements of  $w$ , in a case where the initial errors, drift, measurement and actuator noise were consistent with Tables 1 and 2. But – what are the limiting factors in this performance? Will the test work when measurements are noisier? What if the ACFs are continuously drifting? To answer these and other questions over a broad range of conditions, we perform Monte Carlo analysis, varying some of the input statistics, creating many different realizations of the errors, running a simulated test for each, and then plotting the statistics of the results.

An example is provided in Figs. 7 and 8, where all error statistics were left constant except the ACF drift parameters. These were varied in increments between 10 nrad and 1 mrad for drift (left plot) and between 1 nm and 100  $\mu$ m for piston (right plot) (1 sigma). Fifty separate random realizations were run for each data point. Several trends are obvious. The first is that WF error, both estimated and actual, grows as the drift grows. The second is an error floor for the actual WF, set by the ACF actuation error at about 8  $\mu$ m. The third is an error floor for the telescope-only (“on-orbit”) WF estimation error, at about 20 nm. Good estimation performance is obtained for drift error sigmas of < 40 nrad and < 50 nm per measurement interval for tilt and piston respectively. Fortunately, the drift sigmas can be kept small by keeping the time between measurements small, by making frequent measurements between control steps.

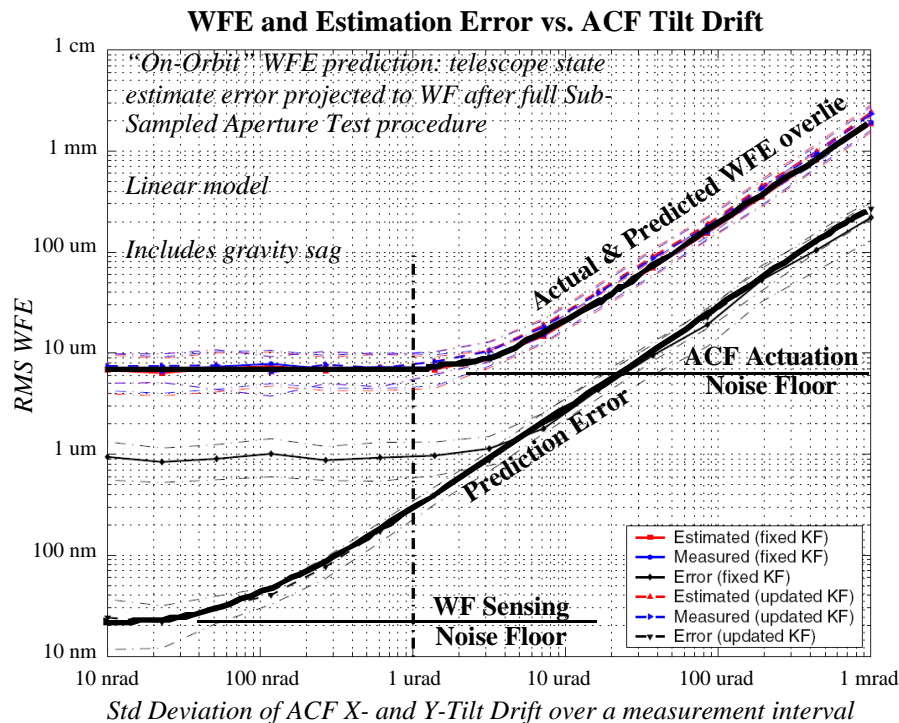


Fig. 7. Monte Carlo results showing WF and WF estimation performance as a function of ACF tilt drift sigmas.

As depicted in Fig. 9, the noise floors were further explored, again using Monte Carlo analysis, applying the nominal conditions of Tables 1 and 2, and varying the WF measurement error (left plot) and the ACF actuation error (right plot). The nominal error points in each case are indicated by arrows.

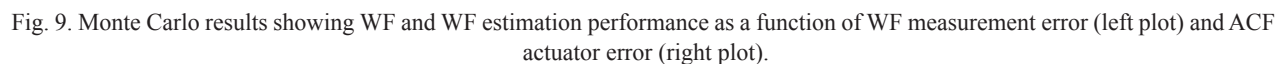
Good performance for WF estimation error seems to require 3 nm sensing error or better. Keeping in mind that the sensing error model is preliminary and approximate until test data is forthcoming from the CoCI and FPI, this still is a tight performance requirement, especially given the very large piston errors that must be accurately resolved at the same time. Nonetheless, it is within the expected performance capabilities of the instruments.

Varying the ACF actuation noise affects the actual WF error, but not the estimation error, again as a consequence of our preliminary sensing error model, which does not reduce sensing accuracy even with large segment piston errors.

Figure 10 is a log-log plot titled "WF and Estimation Error vs. ACF Piston Drift". The y-axis represents "RMS WFE" ranging from 10 nm to 1 cm. The x-axis represents "Std Deviation of ACF Piston Drift over a measurement interval" ranging from 10 nm to 1 mm. The plot shows several curves: a solid black line for "ACF Actuation", a dashed black line for "Noise Floor", a solid black line for "Prediction Error", and a solid black line for "Actual & Predicted WFE overlie". Annotations include "50 Monte Carlo trials per data point", "3 nm WF sensing error", and "1 μm ACF actuation error". A legend in the bottom right corner identifies the line styles for fixed and updated Kalman Filter (KF) results: Estimated (fixed KF) (red solid line), Measured (fixed KF) (blue solid line), Error (fixed KF) (black solid line), Estimated (updated KF) (red dashed line), Measured (updated KF) (blue dashed line), and Error (updated KF) (black dashed line).

## CONCLUSION

The OSE provides a versatile and powerful method for deducing the underlying optical state of a telescope using diverse wavefront and other data. Our analysis of the JWST sub-sampled aperture testing demonstrated OSE operation and feasibility at a simplified level. Further work is underway to improve the detail of the models, to further develop the OSE for Plum Brook testing, and to refine the testing procedures and requirements.



## ACKNOWLEDGEMENT

This work was performed at the Jet Propulsion Laboratory, California Institute of Technology, under contract with the National Aeronautics and Space Administration.

## REFERENCES

1. D.S. Acton, M. Cermak, L. Kingsbury, F. Shi, D.C. Redding, "James Webb Space Telescope Wavefront Sensing and Control Algorithms," Proc. SPIE 5487 (2004).
2. David C. Redding, Fang Shi, Scott A. Basinger, David Cohen, Joseph J. Green, Andrew E. Lowman, Catherine M. Ohara, "Wavefront Control for Large Space Optics," IEEE Aerospace Conference (2003).
3. D. Redding, S. Basinger, D. Cohen, J. Green, A. Lowman, C. Ohara, F. Shi, C. Bowers, R. Burg, L. Burns, B. Dean, "Next Generation Space Telescope Wavefront Sensing and Control," Proc. SPIE 4850 (2002).
4. *MACOS Manual*, JPL document (1998).
5. D. Redding and W. Breckenridge, "Linearized Ray-Trace Analysis," *Selected SPIE Papers on CD ROM, Volume 2, Lens Design*, D. O'Shea, ed. (1998).
6. D. Redding, "JWST Hexapod Control Study Summary Report," JPL document (2003).
7. G. Golub and C. Van Loan, *Matrix Computations*, second edition, (1989).
8. A.E. Bryson and Y.C. Ho, *Applied Optimal Control*, Hemisphere Press (1975).
9. D. Redding, S. Basinger, R. Dekany, G. Brack, B. Oppenheimer, "Adaptive Optics Reconstruction Utilizing Super-Sampled Deformable Mirror Influence Functions," SPIE paper (1998).